The Astrophysical Journal, 978:83 (15pp), 2025 January 01 https://doi.org/10.3847/1538-4357/ad9390

Mapping the Dense Molecular Gas toward 13 Supernova Remnants

Tian-Yu Tu (涂天宇)[1], Yang Chen (陈阳)[1,2], and Qian-Cheng Liu (刘前程)[1]
[1] School of Astronomy & Space Science, Nanjing University, 163 Xianlin Avenue, Nanjing 210023, People's Republic of China; ygchen@nju.edu.cn
[2] Key Laboratory of Modern Astronomy and Astrophysics, Nanjing University, Ministry of Education, Nanjing 210023, People's Republic of China
Received 2024 September 6; revised 2024 November 13; accepted 2024 November 13; published 2024 December 26

Abstract

Supernova remnants (SNRs) can exert strong influence on molecular clouds (MCs) through interaction by shock wave and cosmic rays. In this paper, we present our mapping observation of HCO^+ and HCN 1–0 lines toward 13 SNRs interacting with MCs, together with archival data of CO isotopes. Strong HCO^+ emission is found in the fields of view of SNRs W30, G9.7−0.0, Kes 69, 3C 391, 3C 396, W51C, HC 40, and CTB109 in the local-standard-of-rest velocity intervals in which they are suggested to show evidence of SNR–MC interaction. We find an incomplete ^{12}CO shell surrounding G9.7−0.0 with an expanding motion. This shell may be driven by the stellar wind of the SNR progenitor. We also find an arc of ^{12}CO gas spatially coincident with the northwestern radio shell of Kes 69. As for the HCO^+ line emission, SNRs 3C 391 and W51C exhibit significant line profile broadening indicative of shock perturbation, and CTB109 exhibits a possible blueshifted line wing brought by shock interaction. We do not find significant variation of the $I(HCO^+)/I(HCN)$ line ratio between broad-line and narrow-line regions, among different SNRs, and between MCs associated with SNRs and typical Galactic MCs. Therefore, we caution on using the $I(HCO^+)/I(HCN)$ line ratio as a diagnostic of SNR feedback and cosmic-ray (CR) ionization. We also estimate the $N(HCO^+)/N(CO)$ abundance ratio in 11 regions toward the observed SNRs, but they show little difference from the typical values in quiescent MCs, possibly because $N(HCO^+)/N(CO)$ is not an effective tracer of CR ionization.

Unified Astronomy Thesaurus concepts: Molecular clouds (1072); Supernova remnants (1667)

1. Introduction

Massive ($\gtrsim 8M_{\odot}$) stars, born in molecular clouds (MCs) and ending their lives as supernovae (SNe), each redeposit $\sim 10^{51}$ erg back to the interstellar medium and regulate the galactic ecology and evolution (A. Pillepich et al. 2018). Many supernova remnants (SNRs) are found to be located in the vicinity of MCs (e.g., B. Jiang et al. 2010; Y. Chen et al. 2014). If an SNR is interacting with an MC, the shock, X-ray emission, and the cosmic rays (CRs) accelerated by the SNR can strongly affect the physical and chemical properties of the MC (J. Vink 2020), which can be observed in terms of molecular transitions.

CO and its isotopes are the most popular molecular species employed to investigate the SNR–MC interaction (e.g., X. Zhou et al. 2023), which can be evidenced by morphology alignment of the CO emission with the SNR radio emission, and the line broadening or line wings (e.g., Y. Su et al. 2009; X. Zhou et al. 2009; B. Jiang et al. 2010; X. Zhou et al. 2016b). However, the CO molecules can only trace the most extended and low-density (with a critical density[3] of $\sim 2 \times 10^3$ cm^{-3} for the 1–0 line and 3×10^4 cm^{-3} for the 3–2 line at 10 K) part of the MCs. Although denser shocked gas with broadened line profiles has been found in several SNRs (e.g., B.-C. Koo & D.-S. Moon 1997; W. T. Reach & J. Rho 1999; W. T. Reach et al. 2005; J.-J. Lee et al. 2012), mapping observations of dense molecular gas around SNRs are still lacking.

The HCO^+ and HCN 1–0 lines, with critical densities of $\sim 2 \times 10^5$ cm^{-3} and 10^6 cm^{-3}, respectively, are typical dense gas tracers in MCs (Y. L. Shirley 2015). The integrated intensity ratio of the two lines (hereafter called line ratio for simplicity) have been used as diagnostics of physical processes in extragalactic studies (e.g., M. Krips et al. 2008; F. Costagliola et al. 2011). A simultaneous mapping of CO and these two dense gas tracers can provide a comprehensive view of the molecular environment of SNRs.

SNRs are believed to be the main accelerators of Galactic CRs (e.g., F. A. Aharonian 2013). The high-energy (with kinetic energy $\gtrsim 280$ MeV) CR protons can generate γ-ray emission originated from the decay of π^0 mesons produced in the collision between the high-energy CR protons and H nuclei in MCs, which is called the hadronic scenario. The high-energy CR electrons can produce γ-ray emission via the inverse Compton scattering of background radiation, which is called the leptonic scenario. The γ-ray emission can be detected by instruments such as the Fermi Large Area Telescope (F. Acero et al. 2016). On the other hand, the low-energy CR protons serve as the main source of ionization in dark MCs shielded from UV radiation (M. Padovani et al. 2009). This process starts the formation of polyatomic molecules in MCs and regulates the molecular chemistry in MCs.

Direct estimation of CR ionization rates in MCs associated with SNRs typically uses the $N(HCO^+)/N(CO)$ and $N(DCO^+)/N(HCO^+)$ abundance ratios (C. Ceccarelli et al. 2011; S. Vaupré et al. 2014). Although the emission of DCO^+ is hard to detect, both observations obtained enhanced CR ionization rates. The enhanced CR ionization rates induced by SNRs can also be revealed indirectly by various observations, including 1720 MHz OH masers and the 6.4 keV Fe I Kα line.

[3] The definition of critical density of a molecular transition is not consistent in a variety of the literature. Here we define it as the Einstein A coefficient divided by the collisional rate coefficient at a specific temperature. The coefficients are taken from the Leiden Atomic and Molecular Database (LAMDA): https://home.strw.leidenuniv.nl/~moldata/.

The production of the 1720 MHz OH masers requires an enhanced CR ionization rate in addition to SNR–MC interaction (P. Lockett et al. 1999; M. Wardle & F. Yusef-Zadeh 2002). The Fe I Kα line is produced via inner-shell ionization of neutral iron when protons in the MeV band collide with MCs (K. K. Nobukawa et al. 2018). Detection of hadronic γ-ray emission also hints that low-energy CR protons are possibly also accelerated and ionizing the MCs.

The HCO^+ molecule has been expected to be a tracer of the CR ionization rate in MCs (C. Ceccarelli et al. 2011; E. Bayet et al. 2011; T. Albertsson et al. 2018). Specifically, enhanced abundance of HCO^+ relative to CO due to CR ionization in shocked MCs has been found in SNRs W49B and W28 (P. Zhou et al. 2022; T.-Y. Tu et al. 2024a) Therefore, observation of HCO^+ in MCs associated with SNRs may provide information about the CR acceleration and ionization in SNRs.

In this paper, we performed new mapping observations in HCO^+ and HCN 1–0 lines, supplemented by archival data of CO isotopes, toward a sample of 13 SNRs suggested to be interacting with MCs in order to obtain the spatial distribution of dense molecular gas around them, to search for shocked dense gas with line profiles broadened, and to study the viability of the $I(\mathrm{HCO}^+)/I(\mathrm{HCN})$ line ratio and the $N(\mathrm{HCO}^+)/N(\mathrm{CO})$ abundance ratio as diagnostics of SN feedback and CR ionization.

The paper is structured as follows. In Section 2, we describe our new observations and other archival data. We present the observational results in Section 3 and discuss the SNR–MC interaction, the $I(\mathrm{HCO}^+)/I(\mathrm{HCN})$ line ratio, and the $N(\mathrm{HCO}^+)/N(\mathrm{CO})$ abundance ratio in Section 4. Finally, a summary is given in Section 5.

2. Observations

2.1. HCO^+ and HCN Observations and Data Reduction

Mapping observations of the 1–0 emission lines of HCO^+ and HCN were performed with the 13.7 m millimeter-wavelength telescope of the Purple Mountain Observatory at Delingha (PMOD; PI: Y. Chen). We included 13 SNRs with evidence of SNR–MC interaction in our observations: W30, G9.7−0.0, G16.7+0.1, Kes 69, Kes 75, 3C 391, Kes 78, 3C 396, 3C 397, W51C, and CTB109 (according to B. Jiang et al. 2010). The HCO^+ and HCN lines were simultaneously observed in 2016–2022. The fast Fourier transform spectrometers with 1 GHz bandwidth and 16,384 channels were used as the back ends, providing a velocity resolution of 0.21 km s^{-1} at 89 GHz. The coverage of the observations is shown in Table 1 where we also list some basic information about the target SNRs. The half-power beamwidth (HPBW) of the telescope at 89 GHz is ≈60″. The main beam efficiencies (within 0.58–0.63 across the years of observation) were corrected according to the annual status reports of PMOD.[4] The raw data were reduced with the GILDAS/CLASS package.[5] The data cubes of HCO^+ and HCN were all resampled to have the same velocity channel width of 0.25 km s^{-1} and the same pixel size of 30″. The rms noise measured in main beam temperature (T_{mb}) is ∼0.05 K for CTB109 and ∼0.1 K for the other SNRs.

2.2. Other Archival Data

Additional data of the 1–0 line of CO isotopes were retrieved from the FOREST Unbiased Galactic plane Imaging survey with the Nobeyama 45 m telescope (FUGIN; T. Umemoto et al. 2017) and Milky Way Image Scroll Painting (MWISP; Y. Su et al. 2019). The FUGIN project covers $|b| \leqslant 1°$, $10° \leqslant l \leqslant 50°$, and $198° \leqslant l \leqslant 236°$. It has an angular resolution of ≈20″, a sensitivity of ∼1–3 K at a velocity channel width of 0.65 km s^{-1} for ^{12}CO, and a sensitivity of ∼0.6–1.5 K at a velocity channel width of 0.65 km s^{-1} for ^{13}CO and C^{18}O. The MWISP project has covered $|b| \leqslant 5°$ and $-10° \leqslant l \leqslant +250°$ with the 1–0 lines of ^{12}CO, ^{13}CO, and C^{18}O and has an angular resolution of ≈50″, a sensitivity of ∼0.5 K at a velocity channel of 0.16 km s^{-1} for ^{12}CO, and a sensitivity of ∼0.3 K at a velocity channel of 0.17 km s^{-1} for ^{13}CO and C^{18}O. Specifically, we used the MWISP data for SNRs W30, G9.7−0.0, HC 40, and CTB109, while the FIGIN data were used for the other SNRs. All the data cubes of CO lines were smoothed to an angular resolution of 60″ so as to have better comparison with the HCO^+ and HCN data.

Data of the radio continuum of the SNRs were taken from the "SNRcat" SNR catalog[6] (G. Ferrand & S. Safi-Harb 2012) and the VLA Galactic Plane Survey (VGPS; J. M. Stil et al. 2006) project to delineate the boundary of the SNRs.

All the processed data were further analyzed with Python packages Astropy (Astropy Collaboration et al. 2018, 2022) and Spectral-cube (A. Ginsburg et al. 2015). The data cubes were reprojected with the Montage[7] package when necessary. We visualized the data with the Python package Matplotlib.[8]

3. Results

3.1. Observational Results of HCO^+ and HCN

The local-standard-of-rest (LSR) velocity intervals in which the observed SNRs are interacting with MCs are listed in Table 1. We detected strong emission of HCO^+ in the fields of view (FOVs) of SNRs W30, G9.7−0.0, Kes 69, 3C 391, 3C 396, W51C, HC 40, and CTB109 in the velocity intervals in which previous studies have found evidence of SNR–MC interaction. In Kes 78, we only detected weak HCO^+ emission, while no HCO^+ and HCN emission was found in SNRs G16.7+0.1, 3C 397, Kes 75, and CTB87 in corresponding velocity intervals.

In Figure 1, we display the integrated intensity maps of HCO^+ in the FOVs of the eight SNRs with strong HCO^+ emission. The spatial distribution of HCN is mostly similar to that of HCO^+. The LSR velocity ranges are consistent with those suggested to exhibit SNR–MC interaction by previous studies. The spectra extracted from the regions marked by black boxes in Figure 1 are shown in Figure 2. Here we briefly describe the observational results of the morphology and spectra of the HCO^+ and HCN emission in the eight SNRs and compare our results with previous studies.

G8.7−0.1 (W30). Our map of W30 is centered on the 1720 MHz OH maser discovered by J. W. Hewitt & F. Yusef-Zadeh (2009), which is located in the eastern part of the SNR. The boundary of W30 shown in Figure 1 was taken from Green's catalog of Galactic SNRs.[9] The emission of HCO^+ mainly consists of three parts: a stripe extending southward from the

4 http://www.radioast.nsdc.cn/zhuangtaibaogao.php
5 https://www.iram.fr/IRAMFR/GILDAS/

6 http://snrcat.physics.umanitoba.ca
7 http://montage.ipac.caltech.edu/
8 https://matplotlib.org/
9 https://www.mrao.cam.ac.uk/surveys/snrs/snrs.info.html

Table 1
Basic Information of Target SNRs

Name	Map Size	Velocity of Interaction (Reference)	CR Acceleration[a] (Reference)	HCO^+ Detection[b]
G8.7−0.1 (W30)	$29' \times 28'$	OH maser: $+36$ km s^{-1} (1) molecular lines: $+8$ to $+56$ km s^{-1} (2)	OH (1), Hγ (24)	Y
G9.7−0.0	$24' \times 20'$	OH maser: $+43$ km s^{-1} (1)	OH (1), PHγ (25)	Y
G16.7+0.1	$19' \times 19'$	OH maser: $+20$ km s^{-1} (3) CO 1–0: $+25.1$ to $+25.9$ km s^{-1} (4) broad CO 2–1: $+25$ km s^{-1} (5)	OH (3), Uγ (26)	N
G21.8−0.6 (Kes 69)	$28' \times 28'$	compact OH maser: $+69$ km s^{-1} (3) extended OH maser: $+85$ km s^{-1} (6) CO 1–0: $\sim +85$ km s^{-1} (7)	OH (3, 6), FeK (27)	Y
G29.7−0.3(Kes 75)	$19' \times 19'$	CO 1–0: $+45$ to $+58$ km s^{-1} (8) broad CO 2–1: $+53$ km s^{-1} (5)	Lγ (28)	N
G31.9+0.0 (3C 391)	$18' \times 18'$	OH maser: $+105$ and $+110$ km s^{-1} (9) broad molecular lines: $+105$ km s^{-1} (10) high-J CO lines: $\sim +105$ km s^{-1} (11)	OH (9), FeK (29), Hγ (30), Chem (31)	Y
G32.8−0.1 (Kes 78)	$29' \times 29'$	OH maser: $+86$ km s^{-1} (12) CO 1–0 and 2–1: $\sim +81$ km s^{-1} (13)	OH (12), FeK (27), Uγ (32)	P
G39.2−0.3 (3C 396)	$21' \times 21'$	CO 1–0 and 2–1: $\sim +84$ km s^{-1} (14) broad CO 2–1: $\sim +69$ and $\sim +77$ km s^{-1} (5)	Hγ (33)	Y
G41.1−0.3 (3C 397)	$19' \times 19'$	CO 1–0: $\sim +32$km s^{-1} (15) broad CO 2–1: $\sim +31$ km s^{-1} (5)	Lγ (34)	N
G49.2−0.7 (W51C)	$19' \times 19'$	OH maser: $+71.9$ and $+68.9$ km s^{-1} (3) broad CO and HCO^+: $+80$ to $+120$ km s^{-1} (16) CR ionization: $\sim +70$ km s^{-1} (17) broad molecular lines: $\sim +70$ km s^{-1} (18) SiO emission: $\sim +67$ km s^{-1} (19)	OH (3), FeK (35), Hγ (36), Chem (17)	Y
G54.4−0.3 (HC 40)	$25' \times 25'$	CO 1–0: $+36$ to $+44$ km s^{-1} (20)	—	Y
G74.9+1.2 (CTB87)	$20' \times 21'$	CO 1–0 and 3–2: ~ -58 km s^{-1} (21) CO 1–0: ~ -58 km s^{-1} (22)	Lγ (37)	N
G109.1−1.0 (CTB109)	N[c]: $34' \times 18'$ W[b]: $17' \times 25'$	CO 1–0: ~ -55 km s^{-1} (23)	PHγ (38)	Y

Notes.
[a] Signature of enhanced CR ionization rate. OH: detection of 1720 MHz OH maser. FeK: detection of 6.4 keV Fe I Kα line. Chem: molecular chemistry induced by enhanced CR ionization rate. Hγ: confirmation of hadronic γ-ray emission. Lγ: confirmation of leptonic γ-ray emission. PHγ: detection of γ-ray that is possibly due to the hadronic scenario. Uγ: detection of γ-ray whose origin has not been discussed. — indicates that there is no evidence of CR acceleration.
[b] Whether HCO^+ emission is detected. Y: strong emission of HCO^+ is detected. P: weak HCO^+ emission is detected with limited spatial extent. N: no HCO^+ is detected in the FOV of the SNR.
[c] Two regions of CTB109 are mapped and coadded.

References: (1) J. W. Hewitt & F. Yusef-Zadeh (2009), (2) K. Feijen et al. (2020), (3) A. J. Green et al. (1997), (4) E. M. Reynoso & J. G. Mangum (2000), (5) C. D. Kilpatrick et al. (2016), (6) J. W. Hewitt et al. (2008), (7) X. Zhou et al. (2009), (8) Y. Su et al. (2009), (9) D. A. Frail et al. (1996), (10) W. T. Reach & J. Rho (1999), (11) A. Gusdorf et al. (2014), (12) B. Koralesky et al. (1998), (13) P. Zhou & Y. Chen (2011), (14) Y. Su et al. (2011), (15) B. Jiang et al. (2010), (16) B.-C. Koo & D.-S. Moon (1997), (17) C. Ceccarelli et al. (2011), (18) C. L. Brogan et al. (2006), (19) G. Dumas et al. (2014), (20) N. Junkes et al. (1992), (21) R. Kothes et al. (2003), (22) Q.-C. Liu et al. (2018), (23) M. Sasaki et al. (2006), (24) B. Liu et al. (2019), (25) P. K. H. Yeung et al. (2016), (26) F. Acero et al. (2016), (27) K. K. Nobukawa et al. (2018), (28) S. M. Straal et al. (2023) (29) T. Sato et al. (2014), (30) T. Ergin et al. (2014), (31) T.-Y. Tu et al. (2024b), (32) K. Auchettl et al. (2014), (33) A. Sezer et al. (2020), (34) P. Bhattacharjee et al. (2017), (35) A. Shimaguchi et al. (2022), (36) T. Jogler & S. Funk (2016), (37) L. Saha (2016), (38) D. Castro et al. (2012).

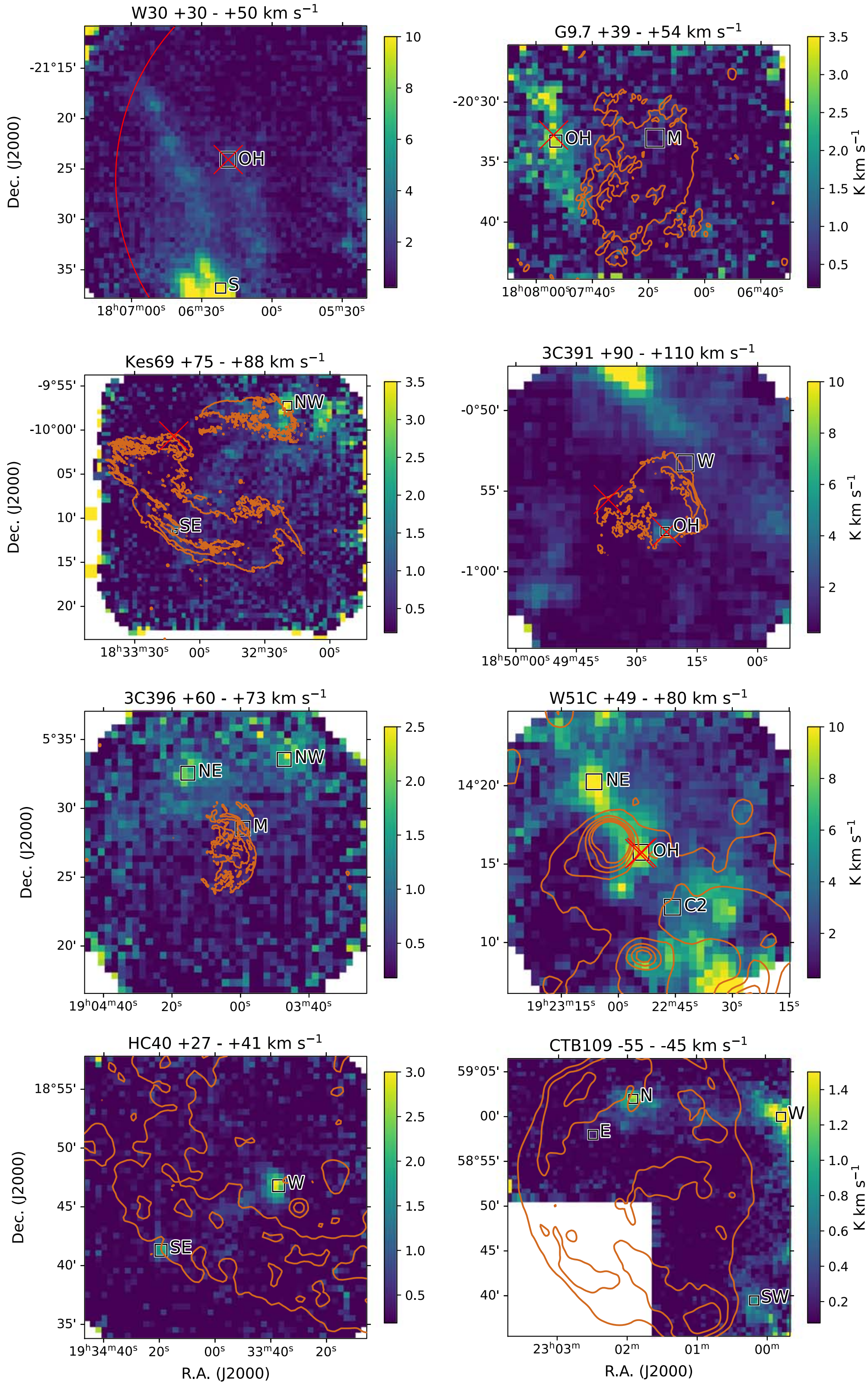

Figure 1. Integrated intensity maps of HCO^+ in the eight SNRs with strong HCO^+ emission. The spectrum extraction portions and the LSR velocity ranges of the integration are labeled at the top of each of the panels. The orange contours show the radio continuum. For W30, we delineate the boundary of the SNR with a red arc. The red crosses shows the 1720 MHz OH masers. The black boxes mark the regions where we extract molecular spectra.

OH maser, another brighter stripe located to the east of the first stripe, and a very bright source containing several HII regions (K. Feijen et al. 2020) in the southern edge of the map. Toward the OH maser, the spectrum of HCO^+ consists of two components centered at $\approx +36$ and $\approx +38$ km s^{-1}, consistent with the ^{13}CO 1–0 line, while in the bright source W30-S, the

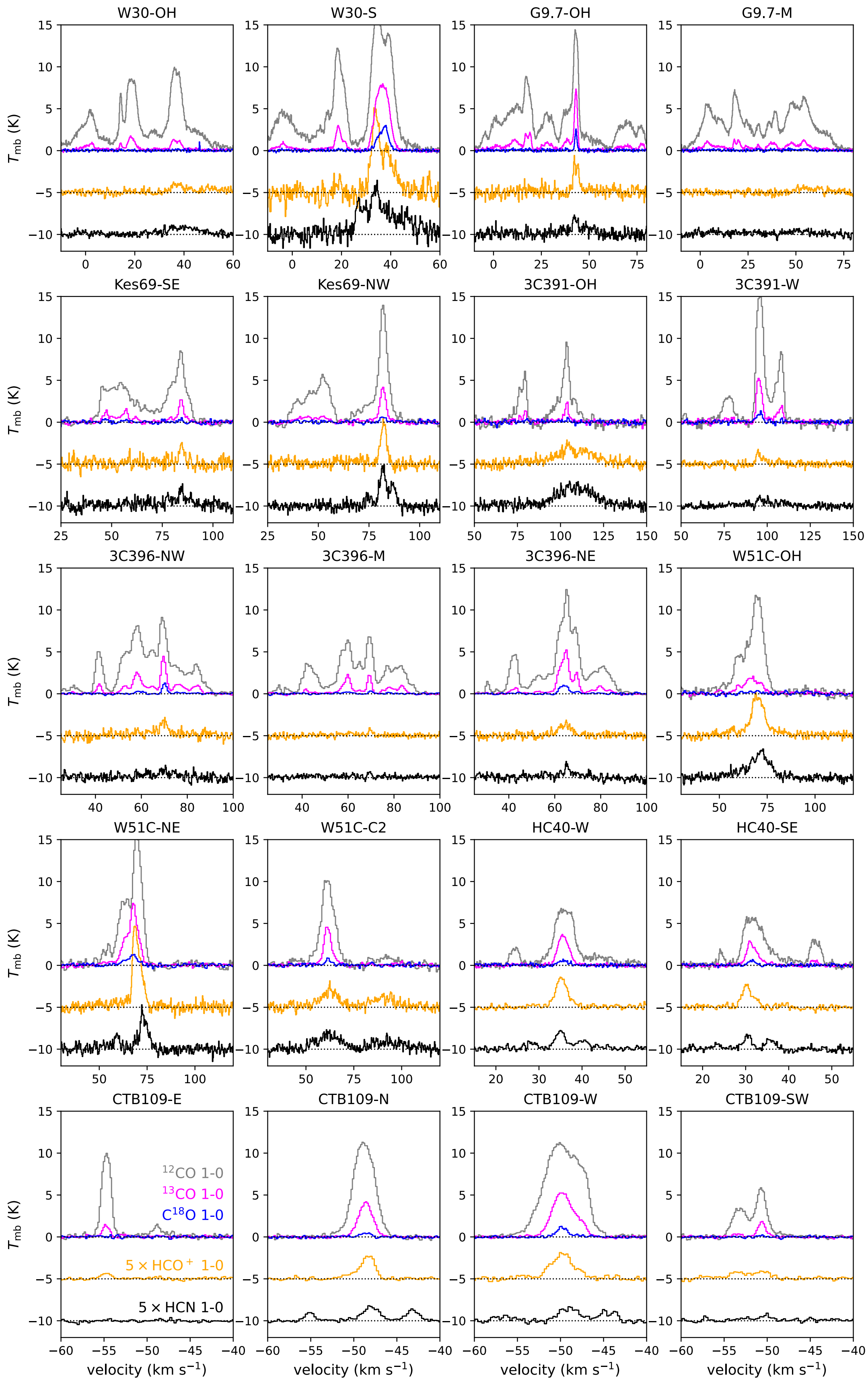

Figure 2. ^{12}CO 1–0 (gray), ^{13}CO 1–0 (magenta), C^{18}O 1–0 (blue), HCO$^+$ 1–0 (orange), and HCN 1–0 (black) spectra averaged in the black boxes in Figure 1. The HCO$^+$ and HCN spectra are multiplied by a factor of 5 and lowered by 5 K and 10 K, respectively, for better visualization.

two components of HCO^+ are located at $\approx +34$ and $\approx +40$ km s^{-1}. All of the velocities are roughly consistent with the systemic velocity of the OH maser (+36 km s^{-1}), suggesting that the dense gas traced by HCO^+ is located at the same distance as W30 or even is the same cloud that harbors the maser.

G9.7−0.0 (hereafter G9.7 for short). Extended HCO^+ emission is located to the east of G9.7 and covers the position of the OH maser. The line profile of HCO^+ toward the OH maser exhibits a double-peak feature, the dip velocity of which is similar to the peak position of ^{13}CO and C^{18}O lines at $\approx +43.4$ km s^{-1}. But at other positions, the systemic velocity of HCO^+ is the same as that of ^{13}CO and C^{18}O ($\sim +43$ km s^{-1}; not shown). We report a marginal detection of HCO^+ inside the SNR (G9.7-M). The seemingly broad line profile of HCO^+ and HCN may be due to different components as shown in the ^{13}CO line.

G21.8−0.6 (Kes 69). HCO^+ emission of Kes 69 is mainly located on the northwestern boundary of the SNR at $\approx +83$ km s^{-1}. Small-scale HCO^+ emission is also found toward the southeastern shell of Kes 69 (see the region Kes 69-SE). The systemic velocity of the HCO^+ and HCN lines ($\approx +85$ km s^{-1}) toward Kes 69-SE is consistent with both of that of the extended OH maser found by J. W. Hewitt et al. (2008) and that of the CO 1–0 and HCO^+ obtained by X. Zhou et al. (2009). We do not detect HCO^+ and HCN emission associated with the OH maser toward the northeast of the SNR at $\sim +69$ km s^{-1}, which is the systemic velocity of the 1720 MHz OH maser found by A. J. Green et al. (1997).

G31.9+0.0 (3C 391). SNR 3C 391 is believed to be interacting with a large MC located toward its west side, which creates the bright radio bar along its western boundary (e.g., W. T. Reach et al. 2002). We find weak HCO^+ emission in this direction (e.g., 3C 391-W), which extends northeastward to reach a star-forming region (J. S. Urquhart et al. 2018) with a strong enhancement in the northern edge of the map. Broadened lines of HCO^+ and HCN are found toward the southern OH maser (i.e., 3C 391-OH), which is consistent with the results of W. T. Reach & J. Rho (1999). We do not detect HCO^+ toward the northeastern OH maser.

G39.2−0.3 (3C 396). Bright HCO^+ emission in the field of view is located outside the northern boundary of the SNR, e.g., region 3C 396-NE at $\approx +66$ km s^{-1} and region 3C 396-NW at $\approx +70$ km s^{-1}. Their large distances from the SNR suggest that they have not yet been hit by the SNR shock. Weak emission of HCO^+ and HCN is detected inside the radio boundary (e.g., region 3C 396-M) at $\approx +70$ km s^{-1}, which is consistent with the results of C. D. Kilpatrick et al. (2016), who found the broadened ^{12}CO 2–1 line to the north of the SNR at +69 km s^{-1}. However, a multiwavelength study suggested that 3C 396 is associated with an MC at $\sim +84$ km s^{-1}(Y. Su et al. 2011).

G49.2−0.7 (W51C). Our map of SNR W51C is centered at the 1720 MHz OH masers (A. J. Green et al. 1997), where (see region W51C-OH) there is a bright HCO^+ emission spot. However, W. W. Tian & D. A. Leahy (2013) argued that the OH masers may result from the HII region, G49.2−0.3, which exhibits a bright radio continuum and is located on the east side of the OH masers. Another HCO^+ spot (W51C-NE) is located to the north of the HII region. Previous studies have found broad molecular lines at both $\sim +70$ km s^{-1}(C. L. Brogan et al. 2013) and $\sim +90$ km s^{-1}(B.-C. Koo & D.-S. Moon 1997). Our results show that the HCO^+ emission is aligned from northeast to southwest across the field of view. Most of the emission is centered at $\sim +70$ km s^{-1}, but the line profiles do not exhibit broadened features at this LSR velocity. The systemic velocities of HCO^+ and HCN toward W51C-NE show a slight difference, and we will further discuss this in Section 4.2. We also find broadened HCO^+ and HCN lines at $\sim +90$ km s^{-1} toward the positions of clump 2 and clump 4 (the former is abbreviated as W51-C2 in Figure 1) reported in B.-C. Koo & D.-S. Moon (1997).

G54.4−0.3 (HC 40). Our observation covers the southeastern part of SNR HC 40. The noticeable emissions of HCO^+ are concentrated in two clumps: HC 40-SE and HC 40-W. HC 40-SE is consistent with the protostellar clump G54.373−0.614 at +31 km s^{-1} (J. S. Urquhart et al. 2018). The asymmetric broad line profile of HCO^+ may be the result of two crowded velocity components. HC 40-W is located at a systemic velocity of $\approx +35$ km s^{-1} and does not exhibit any evidence of star formation (J. S. Urquhart et al. 2018). Weak HCO^+ emission extends from HC 40-W toward southeast.

G109.1−1.0 (CTB 109). The HCO^+ emission in the mapped field of SNR CTB 109 is mainly located in the north, northwest, and southwest of the SNR (see regions CTB109-N, CTB109-NW, and CTB109-SW) and at the LSR velocities centered at −55 to −45 km s^{-1}. Weak HCO^+ emission connects regions CTB109-N and CTB109-W. M. Sasaki et al. (2006) found shocked ^{12}CO 1–0 line toward the "lobe" (approximately CTB109-E in our figure), but we find only weak HCO^+ emission and no evidence of line broadening. However, we find a blueshifted line wing toward CTB109-N, which may be due to the shock interaction. Similar line profile can also be seen, though not that remarkable, in the ^{12}CO emission. Toward CTB109-W, the HCO^+ line, similar to the ^{12}CO and ^{13}CO lines, consists of two velocity components.

3.2. CO toward G9.7 and Kes 69

In this section, we briefly introduce our new results on the spatial distribution of CO gas toward SNRs G9.7 and Kes 69.

G9.7. In the left panel of Figure 3, we show the integrated intensity map of ^{12}CO toward G9.7. Compared with HCO^+ (see Section 3.1 and Figure 1), the emission of ^{12}CO is much more extended. Besides the ^{12}CO gas being spatially coincident with the HCO^+ emission, we also find a "C"-shaped incomplete ^{12}CO shell coincident with the radio continuum of G9.7 in the northern, eastern, and southern parts. The right panel of Figure 3 shows the position–velocity (PV) diagram along the magenta line shown in the left panel. As marked by the dashed magenta ellipse, an annular pattern is located within a velocity between +39 and +47 km s^{-1} and an offset within $0'.10$–$0'.25$, which is often related to the expanding motion of gas (e.g., P. Zhou et al. 2016a).

Kes 69. Figure 4 shows the integrated intensity map of ^{12}CO toward Kes 69. Although X. Zhou et al. (2009) have discussed the ^{12}CO emission associated with Kes 69, their data of the radio continuum suffer from lower sensitivity and do not reveal the radio arc toward the northwestern boundary, but only show a subtle hint there. With the new radio data, we find that a short arc of ^{12}CO emission, together with more compact HCO^+ emission (Kes 69-NW in Figure 1), is spatially coincident with the northwestern radio arc of Kes 69.

4. Discussion

4.1. SNR–MC Interaction

Evidence of SNR–MC interaction includes morphological agreement of molecular lines with SNR emission in the radio or

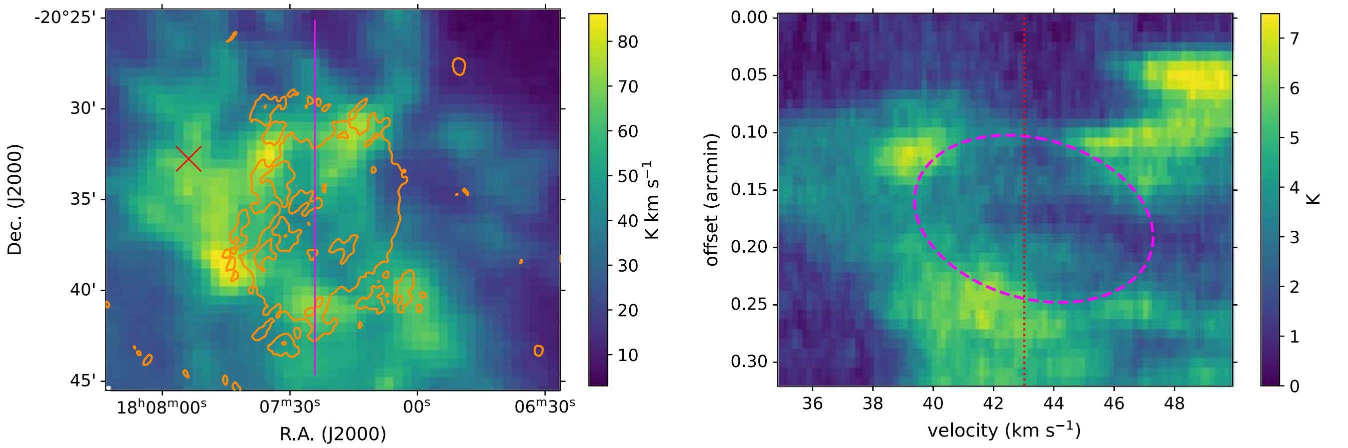

Figure 3. Left panel: integrated intensity map of ^{12}CO toward G9.7 between +39 and +54 km s^{-1}, overlaid with a 327 MHz radio continuum (the level is 40 mJy beam^{-1}). The red cross shows the OH maser detected by J. W. Hewitt & F. Yusef-Zadeh (2009), and the magenta line shows the path along which we extract the position–velocity map. Right panel: position–velocity map of ^{12}CO along the magenta line in the left panel (start from north). The dashed magenta ellipse delineates the possible bubble structure, while the vertical dotted red line shows the systemic velocity of the OH maser (+43 km s^{-1}).

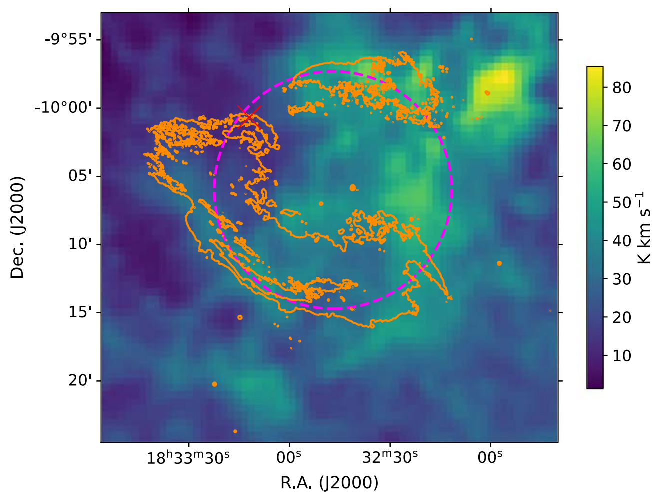

Figure 4. Integrated intensity map of ^{12}CO toward Kes 69 between +75 and +85 km s^{-1}, overlaid with a 1420 MHz radio continuum (the levels are 2 and 8 mJy beam^{-1}). The red cross shows the OH maser detected by A. J. Green et al. (1997). The dashed magenta circle is similar to the circle in Figure 5 of X. Zhou et al. (2009), which shows roughly the molecular arcs associated with Kes 69.

X-ray band, molecular line broadening or asymmetric line profile, 1720 MHz OH masers, line emission with high high-to-low excitation line ratio, etc. (B. Jiang et al. 2010). In this section, we investigate the first two observational facts in our sample of SNRs.

4.1.1. Morphology Agreement of ^{12}CO Molecular Features with SNRs G9.7 and Kes 69

G9.7 was identified by C. L. Brogan et al. (2006) as an SNR and was confirmed to be interacting with MCs by the detection of a 1720 MHz OH maser at +43 km s^{-1} (J. W. Hewitt & F. Yusef-Zadeh 2009). However, no detailed molecular line observation was conducted before. In the left panel of Figure 3, we show an incomplete ^{12}CO shell surrounding the radio boundary of G9.7 (Section 3.2). This suggests that the ^{12}CO shell may be associated with the SNR. The ^{12}CO bubble, expanding at a velocity of ∼4 km s^{-1}, is likely to be driven by the stellar wind of the SNR progenitor. This scenario can be seen in a number of molecular bubbles surrounding SNRs, such as Tycho's SNR (P. Zhou et al. 2016a), VRO 42.05.01 (M. Arias et al. 2019), and Kes 67 (Y.-Z. Shen et al. 2024), with expanding velocities around 5 km s^{-1}.

We note that the OH maser detected by J. W. Hewitt & F. Yusef-Zadeh (2009) seems to be located outside the radio boundary. This may be due to the limited sensitivity of the radio image, since the data of C. L. Brogan et al. (2006) show that the 327 MHz radio continuum extends toward the north-eastern side and approaches the position of the OH maser. The radio morphology in C. L. Brogan et al. (2006) also exhibits an agreement with the HCO$^+$ emission, suggesting possible interaction.

SNR Kes 69 was found to be interacting with the MCs by the detection of both compact OH maser (A. J. Green et al. 1997) and extended OH maser (J. W. Hewitt et al. 2008). The CO emission was reported by X. Zhou et al. (2009), who identified a ^{12}CO arc coincident with the radio arc located in the southeastern boundary of Kes 69. They also plotted a ^{12}CO arc located toward the northwest of Kes 69, but limited by the sensitivity of the radio data, the coincidence of the arc and the radio shell was confused with an HII region G21.902−0.368. The new radio data clearly show a radio shell toward the northwest of Kes 69, making up a circle (similar to that in Figures 4 and 5 in X. Zhou et al. 2009) together with the southeastern radio shell (see Figure 4). Considering that the northwestern ^{12}CO emission is located at a similar velocity to the southeastern ^{12}CO shell (∼+81 km s^{-1}), we suggest that, in addition to the known molecular shell along the southeastern boundary of the SNR, there is also a molecular arc along the northwestern boundary.

4.1.2. Line Broadening and Asymmetric Line Profile

Molecular line broadening and asymmetric line profiles have also been regarded as strong evidence of SNR–MC interaction (B. Jiang et al. 2010). This criterion has been widely used in the diagnostics with CO lines: the asymmetric ^{12}CO line together with the nondetection of ^{13}CO has been used to identify the SNR–cloud interaction in SNRs W44 (M. Seta et al. 2004), 3C 396 (Y. Su et al. 2011), HB3 (X. Zhou et al. 2016b), G51.26+0.11 (W.-J. Zhong et al. 2023), etc. However, the CO lines may suffer from line crowding, especially in the inner Galaxy, where multiple emission components of the ^{12}CO 1–0

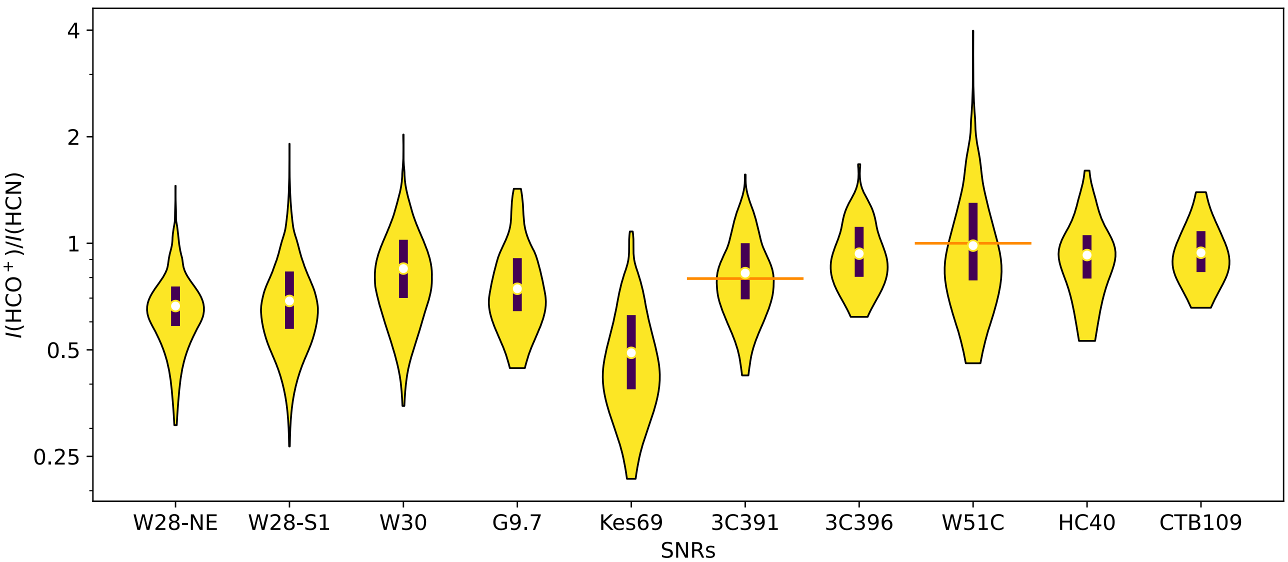

Figure 5. Violin plot showing the ranges of line ratio $I(HCO^+)/I(HCN)$ in the entire FOVs of the eight SNRs and two regions of SNR W28. Mean values are shown with white dots, while quartiles are shown as the two ends of each thick black bar. The two horizontal orange lines show the $I(HCO^+)/I(HCN)$ of the broadened lines toward 3C 391-OH and W51C-C2.

line crowd in a small velocity interval, which would confuse the line broadening due to SNR–MC interaction.

Compared with the ^{12}CO 1–0 line, the HCO^+ 1–0 line traces a denser part of molecular cloud and suffers less from line crowding. The HCO^+ 1–0 transition is easy to get optically thick (F. F. S. van der Tak et al. 2007), which allows it to be broadened by shock disturbance. Therefore, broadened HCO^+ 1–0 can also serve as a shock tracer. Among the 13 SNRs we observed, we find shocked HCO^+ toward 3C 391 and W51C (3C 391-OH and W51C-C2; see Figure 2), consistent with the results of W. T. Reach & J. Rho (1999) and B.-C. Koo & D.-S. Moon (1997).

In addition to these two SNRs known to exhibit broadened HCO^+ line, a blueshifted line wing of HCO^+ toward the CTB109-N region is also noticeable. This region is compatible with the X-ray absorption reported by M. Sasaki et al. (2004). If the MC is absorbing the X-ray emission of the SNR, it could be located in front of the SNR. The SNR shock interacting with the MC could drive the molecular gas to move toward us, which results in a blueshifted wing in molecular transitions, as we can see in the HCO^+ 1–0 line. However, we could still not rule out the possibility that the line wing is caused by another component due to the limited signal-to-noise ratio (S/N) of our data. Further high-sensitivity observation is needed to confirm the interaction between CTB109 and its adjacent dense molecular gas.

In the FOVs of other SNRs, we do not detect any shock broadening or line wings brought by the SNRs. However, our observations are limited in sensitivity, and the $\sim 1'$ beam size may also lead to severe beam dilution, both of which could make it difficult for us to detect the shocked HCO^+ and HCN emission. According to P. Zhou et al. (2022), the peak main beam temperature $T_{\rm peak}$ of the shocked HCO^+ emission can be as low as $\sim$0.04 K. Therefore, our observations could have missed some shocked dense gas in the SNRs. Besides, for young SNRs, it is possible that the shock–cloud interaction has too short of a timescale to have caused detectable line broadening (Y. Fukui et al. 2021).

The 1720 MHz OH maser is a strong signpost of SNR–MC interaction (e.g., B. Jiang et al. 2010). This OH satellite line ($^2\Pi_{3/2}$, $J = 3/2$, $F = 2 \rightarrow 1$) maser is pumped by collisions with other molecular species (M. Wardle & F. Yusef-Zadeh 2002). The pumping of these masers requires a moderately high density ($\sim 10^5$ cm^{-3}), warm temperature ($\sim$50–125 K), and high column density of OH ($\sim 10^{-16}$–10^{-17} cm^{-2}) (P. Lockett et al. 1999). The required density is in favor of the excitation of HCO^+ and HCN. However, in our observation, although significant HCO^+ emission is found toward regions W30-OH, G9.7-OH, 3C 391-OH, and W51C-OH, no HCO^+ emission is spatially coincident with the OH masers toward G16.7+0.1, the northeast of Kes 69, the northeast of 3C 391, and Kes 78. Although this may be due to the limited sensitivity of our observation, a more natural explanation is that the OH masers are rather compact ($\sim 10^2$–10^3 au compared with the $1'$ beam of our observation that corresponds to $\sim$1 pc at a distance of 4 kpc; I. M. Hoffman et al. 2005) and only reflect the physical conditions in a very small region. Therefore, it is unreasonable to use the pumping condition of the OH masers to represent the physical properties of the entire MC.

4.2. $I(HCO^+)/I(HCN)$ *Line Ratio*

In Figure 5, we display the violin plot showing the ranges of the line ratio $I(HCO^+)/I(HCN)$ in the FOVs of the eight SNRs with significant HCO^+ emission. The velocity ranges for the integration are chosen so as to cover all the HCO^+ and HCN molecules with suggested interaction with the SNRs, and only points with an $S/N > 5\sigma$ are included. We also show the line ratios toward W28-NE and W28-S1 (see T.-Y. Tu et al. 2024a and Figure 1 therein for the definition of the two small regions: W28-NE is the shocked MC toward SNR W28, while W28-S1 is a complex of MCs exhibiting star-forming activities free from the disturbance of W28). The values of $I(HCO^+)/I(HCN)$ toward 3C 391-OH and W51C-C2, i.e., the two shocked MCs with broadened HCO^+ and HCN lines, are shown by horizontal orange lines.

As can be seen from the figure, the median values of $I(HCO^+)/I(HCN)$ in all of the SNRs fall in 0.65–1.0, except

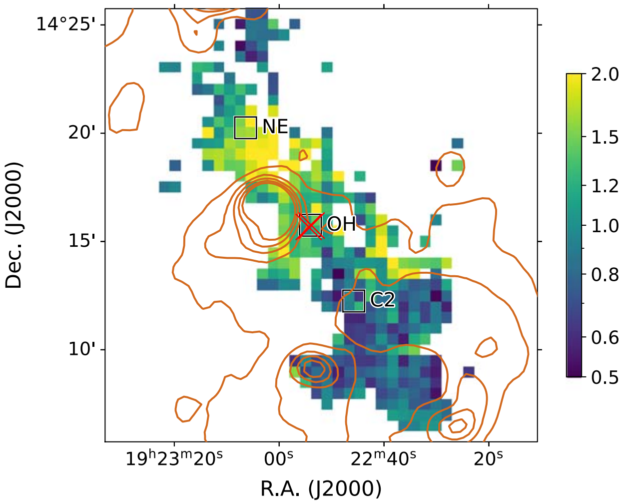

Figure 6. $I(\mathrm{HCO^+})/I(\mathrm{HCN})$ line ratio map toward SNR W51C, overlaid with contours of the VGPS radio continuum in steps of 50, 100, 150, 200, and 250 K. The red crosses show the 1720 MHz OH masers detected by A. J. Green et al. (1997), and the black boxes are the regions where we extract the spectra plotted in Figure 2.

for Kes 69 of which the median value is 0.5. The scatters of the $I(\mathrm{HCO^+})/I(\mathrm{HCN})$ ratios (estimated as the difference between the quartiles and the median values) are all within 0.2, except for W51C of which the upper quartile is 0.3 greater than the median value. The $I(\mathrm{HCO^+})/I(\mathrm{HCN})$ ratios exhibit little difference in shocked (broadened line, in W28-NE, 3C 391-OH, and W51C-C2) and unshocked (narrow-line) clouds and do not show significant variation among SNRs.

The observed region of SNR W51C exhibits the largest dispersion and the highest values of $I(\mathrm{HCO^+})/I(\mathrm{HCN})$. In Figure 6, we show the $I(\mathrm{HCO^+})/I(\mathrm{HCN})$ line ratio map toward W51C. It is clear that the line ratio is higher toward the northeast and lower toward the southwest. To investigate why $I(\mathrm{HCO^+})/I(\mathrm{HCN})$ is enhanced toward the northeastern part of the observed region, we take a closer look at the spectra of W51C-NE and make a grid of $\mathrm{HCO^+}$, HCN, and $\mathrm{C^{18}O}$ spectra in Figure 7.

From the spectra of W51C-NE (Figure 2), we find that the spectrum of $\mathrm{HCO^+}$ is redshifted compared with $\mathrm{C^{18}O}$, while HCN is further redshifted compared with $\mathrm{HCO^+}$. Both $\mathrm{HCO^+}$ and HCN exhibit an asymmetric line profile, with a sharp decrease toward the blue side. Figure 7 shows that the velocity shift of $\mathrm{HCO^+}$ and HCN pervades the entire region with an enhanced $I(\mathrm{HCO^+})/I(\mathrm{HCN})$ line ratio. For the HCN line, we notice a weak component at $\approx +59\,\mathrm{km\,s^{-1}}$ in W51C-NE, which is not consistent with any other components shown in other molecular transitions. The high $I(\mathrm{HCO^+})/I(\mathrm{HCN})$ and velocity shift could be explained by self-absorption of $\mathrm{HCO^+}$ and HCN, which is stronger for the HCN line. The self-absorption is blueshifted so that the resulting spectra are redshifted. In this case, the $+59\,\mathrm{km\,s^{-1}}$ component corresponds to an unabsorbed hyperfine structure of HCN. This scenario is similar to the blue-profile of contracting molecular cloud cores (N. J. Evans 1999), but the "red-profile" in our case indicates expansion (e.g., D. Mardones et al. 1997). The expanding motion could be due to oscillation of the MC triggered by external perturbation (T.-M. Fu et al. 2011) like the heating of the H II region G49.2−0.3 with bright compact radio emission toward the south of W51C-NE (G. Kim et al. 2016). We note that the stronger absorption of HCN than $\mathrm{HCO^+}$ is anomalous because the $\mathrm{HCO^+}$ line tends to be more susceptible to self-absorption (S. Aalto et al. 2015). A possible explanation of our result is that the absorbing layer has an enhanced abundance of HCN, leading to a stronger absorption.

The $I(\mathrm{HCO^+})/I(\mathrm{HCN})$ line ratio has been studied in various astrophysical conditions. This value is ∼1.1 in the Orion B giant molecular cloud (GMC; M. G. Santa-Maria et al. 2023), ∼0.9 in giant molecular filament 54 (GMF54; Y. Wang et al. 2020), ∼1.32 in infrared dark clouds (IRDCs; e.g., X.-L. Liu et al. 2013), ∼2 in MCs in the outer Milky Way (J. Braine et al. 2023), ∼0.6 in the central molecular zone (CMZ) of our Galaxy (e.g., P. A. Jones et al. 2012; M. G. Santa-Maria et al. 2021), ∼0.8 in the star-forming disk of nearby massive spiral galaxies (M. J. Jiménez-Donaire et al. 2019), and varying from ∼0.4 to ∼1.4 in nearby active galaxies (e.g., R. Aladro et al. 2015). Previous studies have found that mechanical heating by SNRs can lead to a high $I(\mathrm{HCO^+})/I(\mathrm{HCN})$ line ratio at low density and a low $I(\mathrm{HCO^+})/I(\mathrm{HCN})$ at high density (A. F. Loenen et al. 2008; F. Costagliola et al. 2011; G. C. Privon et al. 2017). A high CR ionization rate, which is another factor brought by SNRs (e.g., C. Ceccarelli et al. 2011; S. Vaupré et al. 2014), can also enhance the $I(\mathrm{HCO^+})/I(\mathrm{HCN})$ line ratio by altering the abundance ratio between $\mathrm{HCO^+}$ and HCN because the abundance of $\mathrm{HCO^+}$ is expected to be enhanced with a higher CR ionization rate (Y. N. Chin et al. 1997; M. W. Pound & F. Yusef-Zadeh 2018), while HCN is not sensitive to a CR ionization rate (T. Albertsson et al. 2018; J. Holdship & S. Viti 2022). However, we do not find solid evidence of variation in the $I(\mathrm{HCO^+})/I(\mathrm{HCN})$ line ratio induced by SNRs from our observation. The difference in $I(\mathrm{HCO^+})/I(\mathrm{HCN})$ between broad-line and narrow-line emission in W28, 3C 391, and W51C is not significant, suggesting that the heating effect of the shock wave does not have a strong impact on $I(\mathrm{HCO^+})/I(\mathrm{HCN})$. Concerning CRs, which can diffuse or escape from the shock layer and induce ionization in narrow-line regions (C. Ceccarelli et al. 2011; S. Vaupré et al. 2014), we also fail to find a prominent difference in $I(\mathrm{HCO^+})/I(\mathrm{HCN})$ between SNRs and typical MCs, which does not support the enhancement of $I(\mathrm{HCO^+})/I(\mathrm{HCN})$ by CRs.

We note, however, that CR ionization can affect the molecular abundances, but the relation between the abundance ratio and the line ratio is complicated. Besides the abundances of $\mathrm{HCO^+}$ and HCN, the line ratio is also affected by several physical factors such as gas density, temperature, infrared pumping, electron excitation, elemental abundance, etc. (see D. Salak et al. 2018 and references therein). It is also possible that SNRs have similar effects on the brightness of $\mathrm{HCO^+}$ and HCN, particularly in shocked regions, since studies have suggested the chemical similarity between $\mathrm{HCO^+}$ and HCN (e.g., X.-L. Liu et al. 2013). As a result, these effects may be eliminated when calculating the line ratio.

4.3. N(HCO^+)/N(CO) Abundance Ratio

The $N(\mathrm{HCO^+})/N(\mathrm{CO})$ abundance ratio has been found to be enhanced in shocked regions of SNRs (P. Zhou et al. 2022; T.-Y. Tu et al. 2024a). To study this abundance ratio toward the observed SNRs, we select 11 regions among the 20 regions whose spectra are shown in Figure 2. Since the ^{12}CO spectra may contain several velocity components, we discard nine regions where the ^{12}CO spectra are too complicated to be decomposed and where the $\mathrm{HCO^+}$ spectra have too low S/N to

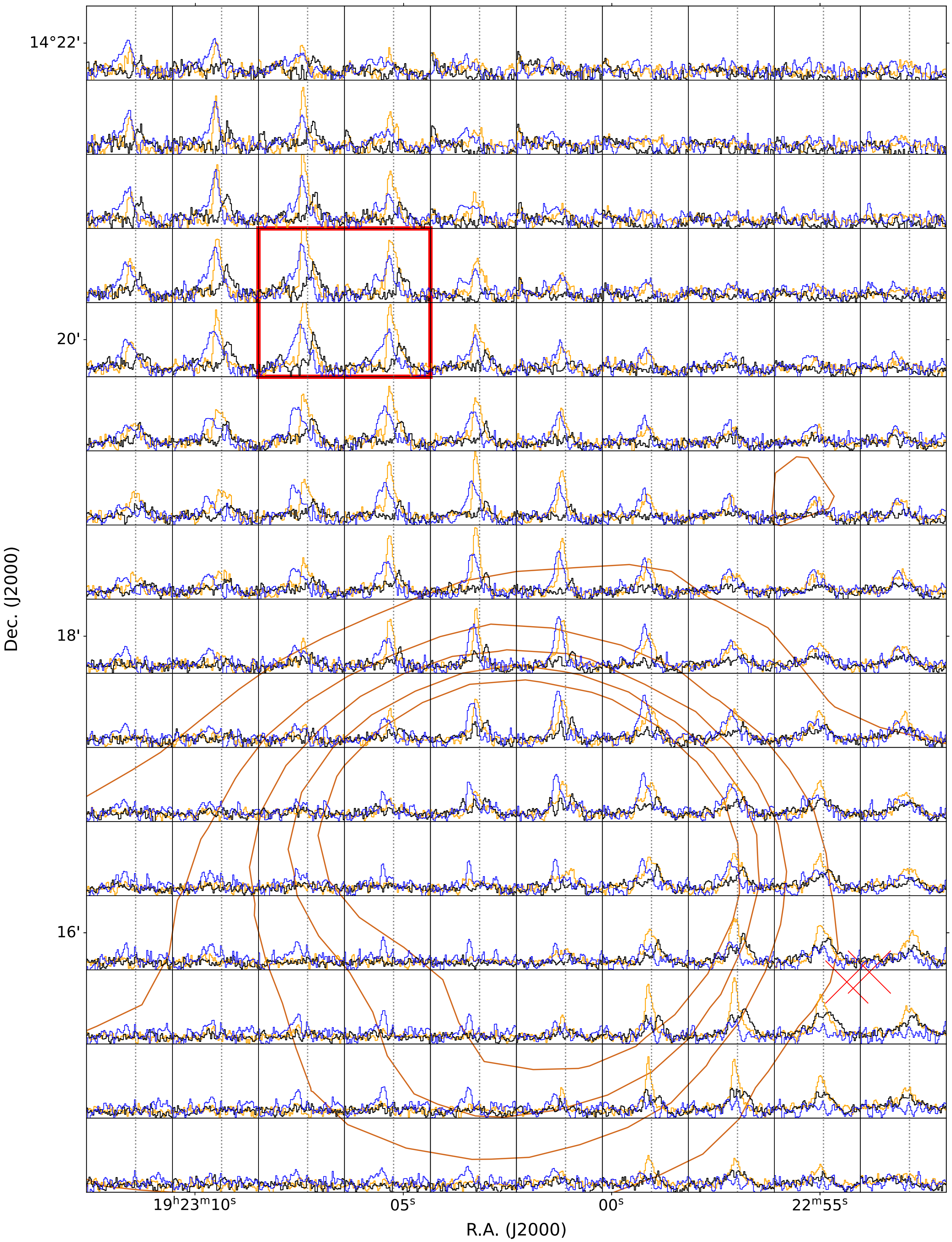

Figure 7. Grid of HCO^+ (orange), HCN (black), and $C^{18}O$ (blue) 1–0 lines around W51C-NE restricted to a velocity range of +50 to +85 km s^{-1} and a T_{mb} range of 0.2–2 K. The orange contours and red crosses are the same as Figure 6. The red box shows the W51C-NE region. The dotted vertical lines show the velocity of +70 km s^{-1} for reference.

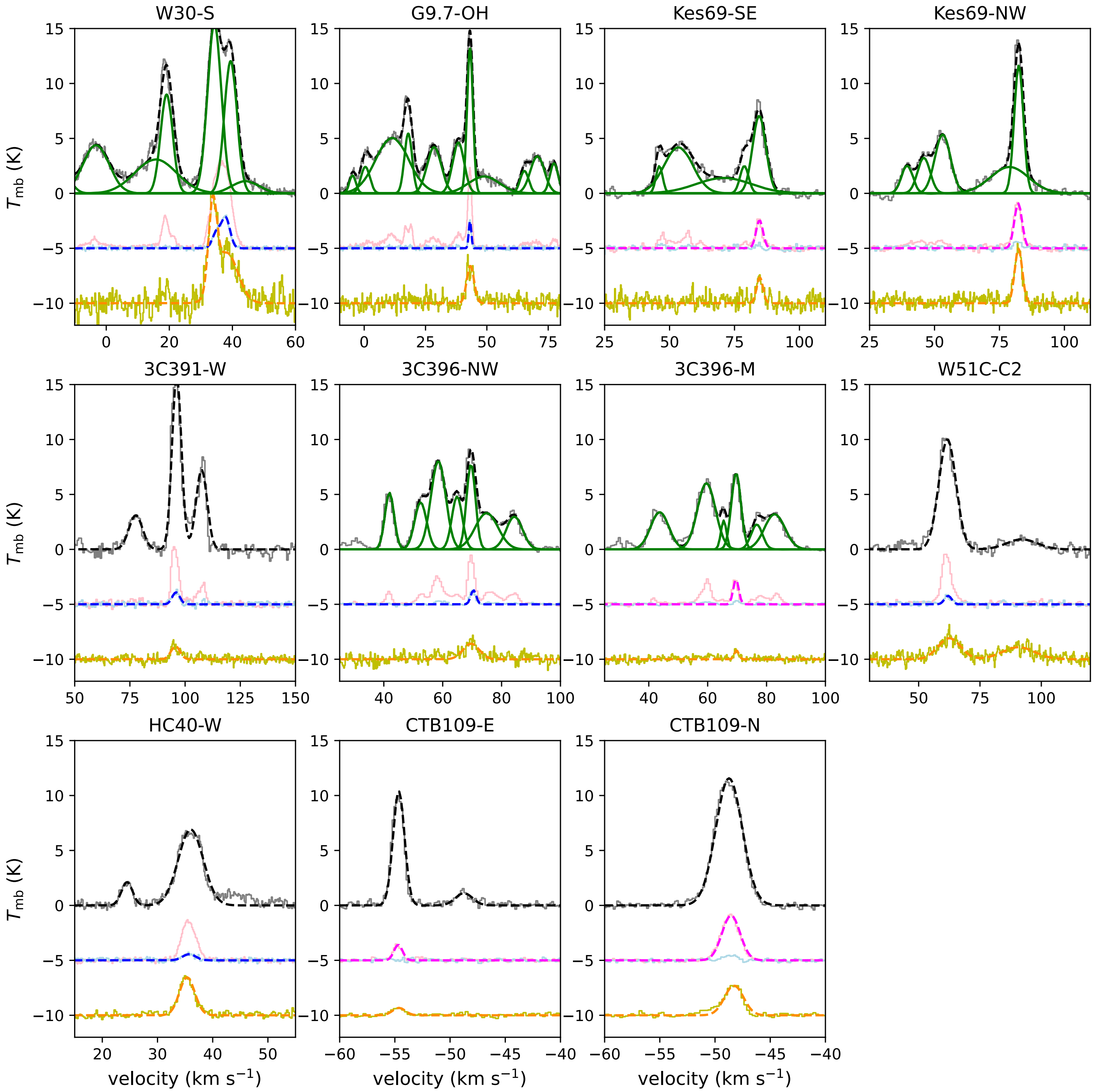

Figure 8. Results of spectral decomposition of ^{12}CO, ^{13}CO, C^{18}O, and HCO$^+$ toward 11 selected regions. The gray, pink, light blue, and yellow lines show the original spectra of ^{12}CO, ^{13}CO, C^{18}O, and HCO$^+$, respectively, while the dashed black, magenta, blue, and orange lines show the corresponding best-fit spectra. The spectra and ^{13}CO, C^{18}O, and HCO$^+$ are lowered by 5 K, 5 K, and 10 K for better visualization. The HCO$^+$ spectra are multiplied by a factor of 5. When the number of ^{12}CO components is greater than 3, the different velocity components are plotted in solid green lines.

be fitted by Gaussian profiles. Toward 3C 391-OH, the broadened ^{12}CO and HCO$^+$ may not trace the same shocked component (T.-Y. Tu et al. 2024b), so we do not further investigate the emission from this region.

We fit the ^{12}CO spectra with multiple Gaussian velocity components. We refer to the peak positions of ^{13}CO and C^{18}O to determine the number and positions of the ^{12}CO components. For the CO isotopes, we fit the C^{18}O spectra when they exhibit high S/N and large line width (FWHM > 5 velocity channel width); otherwise, we fit the ^{13}CO spectra. The procedure of the multi-Gaussian fitting is similar to what we did toward SNR W28 (T.-Y. Tu et al. 2024a). Hereafter, we mainly focus on the components where HCO$^+$ emission is detected and consistent with the systemic velocity of the SNR.

The results of the spectral decomposition are shown in Figure 8 and Table 2. The HCO$^+$ line toward W30-S consists of two velocity components, and both are shown. In several regions, broadened components of ^{12}CO are included (e.g., around +71 km s^{-1} toward Kes 69-SE) to better fit the observed spectra, but these may be due to the artifacts and do not necessarily mean shocked components. Some artifacts have also affected the fitting results of HCO$^+$ toward W30-S

Table 2
Results of Spectral Decomposition and Estimation of the Abundance Ratio $N(HCO^+)/N(CO)$.

Region	T_{ex}[a] (K)	Molecule	v_0[b] (km s^{-1})	T_{peak} (K)	FWHM (km s^{-1})	N (cm^{-2})	$N(HCO^+)/N(CO)$[c]
W30-S[d]	18.9	^{12}CO	34.29 ± 0.05	15.44 ± 0.18	5.12 ± 0.09	2.5×10^{17}	3.2×10^{-5}
		$C^{18}O$	34.95 ± 0.22	1.43 ± 0.13	3.09 ± 0.29	6.4×10^{15}	
		HCO^+	33.72 ± 0.07	1.54 ± 0.14	3.10 ± 0.27	8.0×10^{12}	
	15.5	^{12}CO	39.43 ± 0.05	12.04 ± 0.30	4.72 ± 0.18	1.6×10^{17}	6.9×10^{-5}
		$C^{18}O$	37.88 ± 0.12	2.73 ± 0.12	3.21 ± 0.16	1.2×10^{16}	
		HCO^+	38.18 ± 0.50	0.92 ± 0.05	8.34 ± 0.84	1.1×10^{13}	
G9.7-OH	16.6	^{12}CO	43.13 ± 0.02	13.20 ± 0.17	2.82 ± 0.04	1.1×10^{17}	3.3×10^{-5}
		$C^{18}O$	43.14 ± 0.01	2.46 ± 0.06	1.25 ± 0.03	4.3×10^{15}	
		HCO^+	43.28 ± 0.04	0.68 ± 0.04	3.53 ± 0.22	3.6×10^{12}	
Kes 69-SE	10.4	^{12}CO	84.50 ± 0.17	7.06 ± 0.31	6.03 ± 0.44	1.1×10^{17}	1.4×10^{-5}
		^{13}CO	84.64 ± 0.10	2.57 ± 0.17	3.14 ± 0.23	9.9×10^{15}	
		HCO^+	84.75 ± 0.13	0.47 ± 0.04	2.90 ± 0.31	1.6×10^{12}	
Kes 69-NW	15.1	^{12}CO	82.44 ± 0.04	11.64 ± 0.28	4.14 ± 0.12	1.3×10^{17}	3.8×10^{-5}
		^{13}CO	82.21 ± 0.05	4.09 ± 0.12	3.55 ± 0.12	2.0×10^{16}	
		HCO^+	82.32 ± 0.06	0.99 ± 0.03	3.44 ± 0.14	4.9×10^{12}	
3C 391-W	19.3	^{12}CO	96.21 ± 0.04	15.82 ± 0.25	4.97 ± 0.09	2.5×10^{17}	7.6×10^{-6}
		$C^{18}O$	95.90 ± 0.18	1.09 ± 0.10	4.07 ± 0.42	6.4×10^{15}	
		HCO^+	95.60 ± 0.18	0.24 ± 0.02	4.81 ± 0.44	1.9×10^{12}	
3C 396-NW	11.1	^{12}CO	69.61 ± 0.15	7.76 ± 1.66	3.54 ± 0.54	7.0×10^{16}	3.1×10^{-5}
		$C^{18}O$	70.46 ± 0.05	1.29 ± 0.06	2.14 ± 0.11	3.2×10^{15}	
		HCO^+	69.63 ± 0.24	0.28 ± 0.02	6.50 ± 0.57	2.2×10^{12}	
3C 396-M	10.3	^{12}CO	69.67 ± 0.09	6.94 ± 0.29	3.82 ± 0.27	6.4×10^{16}	5.6×10^{-6}
		^{13}CO	69.61 ± 0.09	2.28 ± 0.20	2.22 ± 0.22	6.1×10^{15}	
		HCO^+	69.81 ± 0.12	0.16 ± 0.02	1.86 ± 0.29	3.6×10^{11}	
W51C-C2	13.4	^{12}CO	61.72 ± 0.06	10.00 ± 0.15	8.26 ± 0.14	2.4×10^{17}	2.3×10^{-5}
		$C^{18}O$	62.01 ± 0.18	0.76 ± 0.08	3.50 ± 0.41	3.2×10^{15}	
		HCO^+	62.49 ± 0.22	0.38 ± 0.02	10.79 ± 0.53	5.5×10^{12}	
HC 40-W	10.2	^{12}CO	36.01 ± 0.03	6.90 ± 0.07	5.32 ± 0.06	7.8×10^{16}	3.6×10^{-5}
		$C^{18}O$	35.74 ± 0.10	0.56 ± 0.04	2.77 ± 0.25	1.7×10^{15}	
		HCO^+	35.36 ± 0.04	0.69 ± 0.02	3.27 ± 0.09	2.8×10^{12}	
CTB109-E	13.8	^{12}CO	−54.64 ± 0.01	10.39 ± 0.10	1.23 ± 0.01	2.5×10^{16}	1.0×10^{-5}
		^{13}CO	−54.69 ± 0.10	1.41 ± 0.07	0.91 ± 0.05	1.6×10^{15}	
		HCO^+	−54.63 ± 0.07	0.14 ± 0.01	1.36 ± 0.16	2.6×10^{11}	
CTB109-N	15.0	^{12}CO	−48.73 ± 0.01	11.56 ± 0.06	2.83 ± 0.02	9.6×10^{16}	1.7×10^{-5}
		^{13}CO	−48.55 ± 0.01	4.08 ± 0.04	1.94 ± 0.02	1.1×10^{16}	
		HCO^+	−48.28 ± 0.02	0.54 ± 0.01	2.01 ± 0.06	1.6×10^{12}	

Notes.
[a] The excitation temperature T_{ex} is obtained from the optically thick ^{12}CO emission. It is assumed to be the same for different species.
[b] Central velocities of the spectral components.
[c] The abundance ratio between HCO^+ and ^{12}CO. The column densities of ^{12}CO are adopted directly from ^{12}CO instead of scaling from ^{13}CO and $C^{18}O$.
[d] The HCO^+ emission toward W30-S consists of two components.

and 3C 396-NW, resulting in broad line profiles. Toward G9.7-OH, the HCO^+ spectrum exhibits a double-peak profile (see Section 3.1), but here we neglect it and fit the entire spectrum with one Gaussian component. Toward W51C-C2, the $+61$ km s^{-1} components of ^{12}CO and HCO^+ also exhibit broaden profiles, but they are caused by multiple velocity components that cannot be distinguished. We will further discuss the molecular clump W51C-C2 in a forthcoming paper with another observation (T.-Y. Tu et al. 2024c). Toward CTB109-N, although we find possible line wing structures of ^{12}CO and HCO^+ (see Section 4.1.2), it is hard to distinguish so we regard the entire spectra as one single component.

To estimate the column densities of CO and HCO^+, we follow the method in J. G. Mangum & Y. L. Shirley (2015) based on the local thermodynamic equilibrium (LTE) assumption. We also assume that the beam filling factor is 1. Since all the relevant ^{12}CO components are consistent with a ^{13}CO or $C^{18}O$ component, the ^{12}CO emission is expected to be optically thick, so the excitation temperature of the ^{12}CO lines can be estimated by

$$T_{ex} = \frac{h\nu/k}{\ln\left(1 + \frac{h\nu/k}{T_{peak} + J_\nu(T_{bg})}\right)}, \quad (1)$$

where $J_\nu(T) = (h\nu/k)/[\exp(h\nu/kT) - 1]$ is the Rayleigh–Jeans equivalent temperature and $T_{\rm bg} = 2.73$ K. In the LTE condition, the excitation temperatures are assumed to be the same for different molecular transitions. The column densities of the species can then be estimated by

$$N = \left(\frac{3h}{8\pi^3 S\mu^2 R_i}\right)\left(\frac{Q_{\rm rot}}{g_I g_J g_K}\right)\left(\frac{\exp(E_{\rm u}/kT_{\rm ex})}{\exp(h\nu/kT_{\rm ex}) - 1}\right) \times \int -\ln\left[1 - \frac{T_{\rm mb}}{J_\nu(T_{\rm ex}) - J_\nu(T_{\rm bg})}\right] dv, \quad (2)$$

where $Q_{\rm rot} \approx kT/hb + 1/3$ is the rotational partition function and other parameters were explained in detail by J. G. Mangum & Y. L. Shirley (2015). The estimated excitation temperatures and column densities are listed in Table 2.

We note that the typical isotope ratios in the Galactic inner disk (2–6 kpc from the Galactic center) are ^{12}C/^{13}C ~ 40 and ^{16}O/^{18}O ~ 327 (Y. T. Yan et al. 2023). However, the isotope ratios of CO we obtained are significantly lower than these typical values (see Table 2). This could be because the optical depths are underestimated in Equation (2). For ^{12}CO, its 1–0 transition tends to be optically thick, so the column densities may be underestimated, while the estimated column densities of ^{13}CO and C^{18}O are closer to the real values than ^{12}CO does because they are almost optically thin. The HCO$^+$ 1–0 line, although much weaker than the ^{12}CO 1–0 line, could also be optically thick even when the column density is not high ($\gtrsim 10^{12}$ cm^{-2}; F. F. S. van der Tak et al. 2007). Therefore, the column densities of HCO$^+$ in Table 2 could also be underestimated. To reduce the uncertainty brought by the underestimation of optical depth in Equation (2) to some extent, we divide N(HCO$^+$) by the N(CO) directly obtained from the ^{12}CO spectra instead of using the CO isotopes scaled with the typical isotope ratios. However, this cannot fully eliminate the uncertainty on optical depth. Another source of uncertainty is the LTE assumption, which may be invalid at low volume densities. Therefore, our calculation of N(HCO$^+$)/N(CO) can only be regarded as a rough order-of-magnitude estimation. The results of our estimation are listed in Table 2. We find that the N(HCO$^+$)/N(CO) in our selected regions are all of orders $\sim 10^{-5}$ or $\sim 10^{-6}$.

Enhanced N(HCO$^+$)/N(CO) has been proposed to be a tracer of enhanced CR ionization rate according to chemical simulations (e.g., E. Bayet et al. 2011; C. Ceccarelli et al. 2011). However, N(HCO$^+$)/N(CO) varies significantly from cloud to cloud, and we do not find a difference between the MCs associated with the SNRs in our sample and typical quiescent MCs ($\sim 10^{-4}$–$\sim 10^{-6}$; e.g., M. Agúndez & V. Wakelam 2013; O. Miettinen 2014; A. Fuente et al. 2019), even if in the SNRs with evidence of enhanced CR ionization rates (e.g., W30, G9.7, Kes 69, 3C 391, 3C 396, W51C, and CTB109 as listed in Table 1). Similarly, in most SNRs with solid evidence of enhanced CR ionization rates, the N(HCO$^+$)/N(CO) abundance ratios ($\sim 4 \times 10^{-5}$ in W51C, C. Ceccarelli et al. 2011; W28, S. Vaupré et al. 2014; $\sim 8 \times 10^{-5}$ in 3C 391, T.-Y. Tu et al. 2024b) do not deviate from the typical values in quiescent MCs. In W51C and W28 where the enhanced CR ionization rates were estimated with both N(HCO$^+$)/N(CO) and N(DCO$^+$)/N(HCO$^+$) (C. Ceccarelli et al. 2011; S. Vaupré et al. 2014), the results were mainly deduced from the unusually low column densities of DCO$^+$ instead of enhanced N(HCO$^+$)/N(CO). Therefore, it appears that N(HCO$^+$)/N(CO) is not an effective tracer of chemistry induced by CRs. Significantly enhanced N(HCO$^+$)/N(CO)($\sim 10^{-3}$) has only been found in SNR W49B (P. Zhou et al. 2022), but this high ratio was discovered in the shocked MC with a broadened molecular line profile where shock chemistry cannot be ignored. Another example is SNR W28, where the N(HCO$^+$)/N(CO) is enhanced in shocked MCs ($\sim 10^{-4}$) compared with unshocked MCs close to the SNR ($\sim 10^{-5}$) (T.-Y. Tu et al. 2024a). It is likely that shock interaction is important for CRs to enhance the N(HCO$^+$)/N(CO) abundance ratio.

We note, from Table 1, that in most SNRs with signatures of enhanced CR ionization rates, HCO$^+$ emission is detected (W30, G9.7, Kes 69, 3C 391, Kes 78, W51C, and CTB109). This suggests that the detection of HCO$^+$ indicates the presence of the target MCs to produce hadronic γ-rays. However, there are cases where HCO$^+$ is detected with no evidence of enhanced CR ionization (HC40) and where no HCO$^+$ is detected but solid evidence of enhanced CR ionization has been observed (G16.7+0.1). Therefore, whether HCO$^+$ can be detected depends strongly on the local environment of the SNR, especially the gas density and temperature, instead of whether the CR ionization rate is enhanced to elevate the abundance of HCO$^+$.

X-rays from the SNRs can also lead to enhanced ionization rates in MCs (P. R. Maloney et al. 1996; S. Viti 2017). However, according to the estimation of T.-Y. Tu et al. (2024b), the X-ray ionization rate induced by SNR 3C 391 is negligible. Since 3C 391 is a bright SNR in the X-ray band and the other SNRs we observe do not show significantly high X-ray luminosities (e.g., C. Albert & V. V. Dwarkadas 2022), we consider that X-ray ionization in the target SNRs can be ignored.

5. Conclusion

In this paper, We present our observation of HCO$^+$ and HCN 1–0 lines toward 13 SNRs interacting with MCs with the PMO 13.7 m telescope, supplemented by archival data of CO isotopes. The results can be summarized as follows:

1. We find strong emission of HCO$^+$ toward the FOVs of SNRs W30, G9.7−0.0, Kes 69, 3C 391, 3C 396, W51C, HC 40, and CTB109 in the velocity intervals proposed to show evidence of SNR–MC interaction. Weak HCO$^+$ emission is detected in Kes 78, while no HCO$^+$ emission is found in G16.7+0.1, 3C 397, Kes 75, and CTB87.

2. We find a ^{12}CO arc surrounding the radio continuum of SNR G9.7−0.0 in the northern, eastern, and southern parts, with an expansion as revealed by the PV diagram around the LSR velocity of the 1720 MHz OH maser. This bubble is likely to be driven by the stellar wind of the SNR progenitor. With the new radio data, we also find a ^{12}CO arc spatially coincident with the northwestern radio arc of Kes 69. This suggests that, in addition to the known molecular shell along the southeastern boundary of the SNR, there is also a molecular arc along the northwestern boundary.

3. Significant shock broadening is found in SNRs 3C 391 and W51C, and CTB109 exhibits a possible blueshifted line wing brought by shock interaction. The line profile toward CTB109-N is consistent with the X-ray absorption. This nondetection of line broadening in other SNRs may be due to the limited sensitivity and angular resolution of our

observation, as well as the possibility that the timescale of the interaction is too short to allow for detectable line broadening. For the 1720 MHz OH masers toward G16.7+0.1, the northeast of Kes 69, the northeast of 3C 391, and Kes 78, we did not find corresponding HCO^+ or HCN emission, probably because the OH masers only take up a rather small physical scale and cannot represent the physical properties of the entire MC.

4. The median values of $I(HCO^+)/I(HCN)$ in all of the SNRs except Kes 69 fall in 0.65–1.0. The highest values and largest scatter of $I(HCO^+)/I(HCN)$ are found in W51C, which may be caused by self-absorption that is affected by expansion motion and is more severe for HCN. We do not find significant variation of $I(HCO^+)/I(HCN)$ between broad-line and narrow-line regions, and among different SNRs. The obtained $I(HCO^+)/I(HCN)$ also deviate little from typical values found in Galactic MCs. The observed $I(HCO^+)/I(HCN)$ line ratio results from a complex interplay of excitation and chemical effects, so we caution on using $I(HCO^+)/I(HCN)$ line ratio as a diagnostic of SNR feedback and CR ionization.

5. We estimate the $N(HCO^+)/N(CO)$ abundance ratio in 11 regions toward the observed SNRs. The abundance ratios $N(HCO^+)/N(CO)$ in all of the selected regions are of orders $\sim 10^{-5}$ or $\sim 10^{-6}$, which is similar to the values in typical quiescent MCs. Combining the $N(HCO^+)/N(CO)$ ratio toward the points with enhanced CR ionization rates in W28, W51C, and 3C 391, we suggest that the $N(HCO^+)/N(CO)$ ratio may not be an effective tracer of CR-induced chemistry.

Acknowledgments

The authors thank the anonymous reviewer for the helpful suggestions. The authors are grateful to the staff of Qinghai Radio Observing Station at Delingha for their help during the observation. T.-Y. Tu thanks Ping Zhou for helpful discussion. Y.C. acknowledges the support from NSFC grants Nos. 12173018, 12121003, and 12393852.

Facilities: PMO:DLH, No: 45 m, VLA.

Software: astropy (Astropy Collaboration et al. 2018, 2022), Spectral-cube (A. Ginsburg et al. 2015), GILDAS (Gildas Team, https://www.iram.fr/IRAMFR/GILDAS/), Montage (http://montage.ipac.caltech.edu/), Matplotlib (https://matplotlib.org).

ORCID iDs

Tian-Yu Tu (涂天宇) https://orcid.org/0000-0002-9776-5610
Yang Chen (陈阳) https://orcid.org/0000-0002-4753-2798
Qian-Cheng Liu (刘前程) https://orcid.org/0000-0002-5786-7268

References

Aalto, S., Martín, S., Costagliola, F., et al. 2015, A&A, 584, A42
Acero, F., Ackermann, M., Ajello, M., et al. 2016, ApJS, 224, 8
Agúndez, M., & Wakelam, V. 2013, ChRv, 113, 8710
Aharonian, F. A. 2013, APh, 43, 71
Aladro, R., Martín, S., Riquelme, D., et al. 2015, A&A, 579, A101
Albert, C., & Dwarkadas, V. V. 2022, MNRAS, 514, 728
Albertsson, T., Kauffmann, J., & Menten, K. M. 2018, ApJ, 868, 40
Arias, M., Domček, V., Zhou, P., & Vink, J. 2019, A&A, 627, A75
Astropy Collaboration, Price-Whelan, A. M., Lim, P. L., et al. 2022, ApJ, 935, 167
Astropy Collaboration, Price-Whelan, A. M., Sipőcz, B. M., et al. 2018, AJ, 156, 123
Auchettl, K., Slane, P., & Castro, D. 2014, ApJ, 783, 32
Bayet, E., Williams, D. A., Hartquist, T. W., & Viti, S. 2011, MNRAS, 414, 1583
Bhattacharjee, P., Majumdar, P., Ergin, T., Saha, L., & Joarder, P. S. 2017, in IAU Symp. 331, Supernova 1987A:30 Years Later - Cosmic Rays and Nuclei from Supernovae and their Aftermaths (Cambridge: Cambridge Univ. Press), 316
Braine, J., Sun, Y., Shimajiri, Y., et al. 2023, A&A, 676, A27
Brogan, C. L., Gelfand, J. D., Gaensler, B. M., Kassim, N. E., & Lazio, T. J. W. 2006, ApJL, 639, L25
Brogan, C. L., Goss, W. M., Hunter, T. R., et al. 2013, ApJ, 771, 91
Castro, D., Slane, P., Ellison, D. C., & Patnaude, D. J. 2012, ApJ, 756, 88
Ceccarelli, C., Hily-Blant, P., Montmerle, T., et al. 2011, ApJ, 740, L4
Chen, Y., Jiang, B., Zhou, P., et al. 2014, in IAU Symp. 296, Supernova Environmental Impacts, ed. A. Ray & R. A. McCray (Cambridge: Cambridge Univ. Press), 170
Chin, Y. N., Henkel, C., Whiteoak, J. B., et al. 1997, A&A, 317, 548
Costagliola, F., Aalto, S., Rodriguez, M. I., et al. 2011, A&A, 528, A30
Dumas, G., Vaupre, S., Ceccarelli, C., et al. 2014, ApJ, 786, L24
Ergin, T., Sezer, A., Saha, L., et al. 2014, ApJ, 790, 65
Evans, N. J., II 1999, ARA&A, 37, 311
Feijen, K., Rowell, G., Einecke, S., et al. 2020, PASA, 37, e056
Ferrand, G., & Safi-Harb, S. 2012, AdSpR, 49, 1313
Frail, D. A., Goss, W. M., Reynoso, E. M., et al. 1996, ApJ, 111, 1651
Fu, T.-M., Gao, Y., & Lou, Y.-Q. 2011, ApJ, 741, 113
Fuente, A., Navarro, D. G., Caselli, P., et al. 2019, A&A, 624, A105
Fukui, Y., Sano, H., Yamane, Y., et al. 2021, ApJ, 915, 84
Ginsburg, A., Robitaille, T., Beaumont, C., et al. 2015, ASP Conf. Ser. Vol.499 (San Francisco: ASP), 363
Green, A. J., Frail, D. A., Goss, W. M., & Otrupcek, R. 1997, AJ, 114, 2058
Gusdorf, A., Güsten, R., Anderl, S., Hezareh, T., & Wiesemeyer, H. 2014, in IAU Symp. 296, Supernova Environmental Impacts, ed. A. Ray & R. A. McCray (Cambridge: Cambridge Univ. Press), 178
Hewitt, J. W., & Yusef-Zadeh, F. 2009, ApJL, 694, L16
Hewitt, J. W., Yusef-Zadeh, F., & Wardle, M. 2008, ApJ, 683, 189
Hoffman, I. M., Goss, W. M., Brogan, C. L., & Claussen, M. J. 2005, ApJ, 620, 257
Holdship, J., & Viti, S. 2022, A&A, 658, A103
Jiang, B., Chen, Y., Wang, J., et al. 2010, ApJ, 712, 1147
Jiménez-Donaire, M. J., Bigiel, F., Leroy, A. K., et al. 2019, ApJ, 880, 127
Jogler, T., & Funk, S. 2016, ApJ, 816, 100
Jones, P. A., Burton, M. G., Cunningham, M. R., et al. 2012, MNRAS, 419, 2961
Junkes, N., Fuerst, E., & Reich, W. 1992, A&AS, 96, 1
Kilpatrick, C. D., Bieging, J. H., & Rieke, G. H. 2016, ApJ, 816, 1
Kim, G., Lee, C. W., Gopinathan, M., Jeong, W.-S., & Kim, M.-R. 2016, ApJ, 824, 85
Koo, B.-C., & Moon, D.-S. 1997, ApJ, 485, 263
Koralesky, B., Frail, D. A., Goss, W. M., Claussen, M. J., & Green, A. J. 1998, AJ, 116, 1323
Kothes, R., Reich, W., Foster, T., & Byun, D.-Y. 2003, ApJ, 588, 852
Krips, M., Neri, R., García-Burillo, S., et al. 2008, ApJ, 677, 262
Lee, J.-J., Koo, B.-C., Snell, R. L., et al. 2012, ApJ, 749, 34
Liu, B., Yang, R.-Z., Sun, X.-N., Aharonian, F., & Chen, Y. 2019, ApJ, 881, 94
Liu, Q.-C., Chen, Y., Chen, B.-Q., et al. 2018, ApJ, 859, 173
Liu, X.-L., Wang, J.-J., & Xu, J.-L. 2013, MNRAS, 431, 27
Lockett, P., Gauthier, E., & Elitzur, M. 1999, ApJ, 511, 235
Loenen, A. F., Spaans, M., Baan, W. A., & Meijerink, R. 2008, A&A, 488, L5
Maloney, P. R., Hollenbach, D. J., & Tielens, A. G. G. M. 1996, ApJ, 466, 561
Mangum, J. G., & Shirley, Y. L. 2015, PASA, 127, 266
Mardones, D., Myers, P. C., Tafalla, M., et al. 1997, ApJ, 489, 719
Miettinen, O. 2014, A&A, 562, A3
Nobukawa, K. K., Nobukawa, M., Koyama, K., et al. 2018, ApJ, 854, 87
Padovani, M., Galli, D., & Glassgold, A. E. 2009, A&A, 501, 619
Pillepich, A., Springel, V., Nelson, D., et al. 2018, MNRAS, 473, 4077
Pound, M. W., & Yusef-Zadeh, F. 2018, MNRAS, 473, 2899
Privon, G. C., Aalto, S., Falstad, N., et al. 2017, ApJ, 835, 213
Reach, W. T., & Rho, J. 1999, ApJ, 511, 836
Reach, W. T., Rho, J., & Jarrett, T. H. 2005, ApJ, 618, 297
Reach, W. T., Rho, J., Jarrett, T. H., & Lagage, P.-O. 2002, ApJ, 564, 302
Reynoso, E. M., & Mangum, J. G. 2000, ApJ, 545, 874
Saha, L. 2016, MNRAS, 460, 3563
Salak, D., Tomiyasu, Y., Nakai, N., et al. 2018, ApJ, 856, 97
Santa-Maria, M. G., Goicoechea, J. R., Etxaluze, M., Cernicharo, J., & Cuadrado, S. 2021, A&A, 649, A32
Santa-Maria, M. G., Goicoechea, J. R., Pety, J., et al. 2023, A&A, 679, A4
Sasaki, M., Kothes, R., Plucinsky, P. P., Gaetz, T. J., & Brunt, C. M. 2006, ApJL, 642, L149

Sasaki, M., Plucinsky, P. P., Gaetz, T. J., et al. 2004, ApJ, 617, 322
Sato, T., Koyama, K., Takahashi, T., Odaka, H., & Nakashima, S. 2014, PASJ, 66, 124
Seta, M., Hasegawa, T., Sakamoto, S., et al. 2004, AJ, 127, 1098
Sezer, A., Ergin, T., Cesur, N., et al. 2020, MNRAS, 492, 1484
Shen, Y.-Z., Chen, Y., Zhang, X., et al. 2024, MNRAS, submitted
Shimaguchi, A., Nobukawa, K. K., Yamauchi, S., Nobukawa, M., & Fujita, Y. 2022, PASJ, 74, 656
Shirley, Y. L. 2015, PASP, 127, 299
Stil, J. M., Taylor, A. R., Dickey, J. M., et al. 2006, AJ, 132, 1158
Straal, S. M., Gelfand, J. D., & Eagle, J. L. 2023, ApJ, 942, 103
Su, Y., Chen, Y., Yang, J., et al. 2009, ApJ, 694, 376
Su, Y., Chen, Y., Yang, J., et al. 2011, ApJ, 727, 43
Su, Y., Yang, J., Zhang, S., et al. 2019, ApJS, 240, 9
Tian, W. W., & Leahy, D. A. 2013, ApJL, 769, L17
Tu, T.-Y., Chen, Y., Zhou, P., Safi-Harb, S., & Liu, Q.-C. 2024a, ApJ, 966, 178
Tu, T.-Y., Rayalacheruvu, P., Majumdar, L., et al. 2024b, ApJ, 974, 262
Tu, T.-Y., Wakelam, V., Chen, Y., Zhou, P., & Zhang, Q.-Q. 2024c, A&A, in press (arXiv:2412.09092)
Umemoto, T., Minamidani, T., Kuno, N., et al. 2017, PASJ, 69, 78
Urquhart, J. S., Konig, C., Giannetti, A., et al. 2018, MNRAS, 473, 1059
van der Tak, F. F. S., Black, J. H., Schöier, F. L., Jansen, D. J., & van Dishoeck, E. F. 2007, A&A, 468, 627
Vaupré, S., Hily-Blant, P., Ceccarelli, C., et al. 2014, A&A, 568, A50
Vink, J. 2020, Physics and Evolution of Supernova Remnants (Berlin: Springer Nature)
Viti, S. 2017, A&A, 607, A118
Wang, Y., Beuther, H., Schneider, N., et al. 2020, A&A, 641, A53
Wardle, M., & Yusef-Zadeh, F. 2002, Sci, 296, 2350
Yan, Y. T., Henkel, C., Kobayashi, C., et al. 2023, A&A, 670, A98
Yeung, P. K. H., Kong, A. K. H., Tam, P. H. T., et al. 2016, ApJ, 827, 41
Zhong, W.-J., Zhang, X., Chen, Y., & Zhang, Q.-Q. 2023, MNRAS, 521, 1931
Zhou, P., & Chen, Y. 2011, ApJ, 743, 4
Zhou, P., Chen, Y., Zhang, Z.-Y., et al. 2016a, ApJ, 826, 34
Zhou, P., Zhang, G.-Y., Zhou, X., et al. 2022, ApJ, 931, 144
Zhou, X., Chen, Y., Su, Y., & Yang, J. 2009, ApJ, 691, 516
Zhou, X., Su, Y., Yang, J., et al. 2023, ApJS, 268, 61
Zhou, X., Yang, J., Fang, M., et al. 2016b, ApJ, 833, 4